

Compressible turbulent convection at very high Rayleigh numbers

Harshit Tiwari^{a,1}, Lekha Sharma^{a,2}, Mahendra K. Verma^{a,3,*}

^a*Department of Physics, Indian Institute of Technology Kanpur, Kanpur 208016, India*

Abstract

Heat transport in highly turbulent convection is not well understood. In this paper, we simulate compressible convection in a box of aspect ratio 4 using computationally-efficient MacCormack-TVD finite difference method on single and multi-GPUs, and reach very high Rayleigh number (Ra)— 10^{15} in two dimensions and 10^{11} in three dimensions. We show that the Nusselt number $Nu \propto Ra^{0.3}$ (classical scaling) that differs strongly from the ultimate-regime scaling, which is $Nu \propto Ra^{1/2}$. The bulk temperature drops adiabatically along the vertical even for high Ra, which is in contrast to the constant bulk temperature in Rayleigh-Bénard convection (RBC). Unlike RBC, the density decreases with height. In addition, the vertical pressure-gradient ($-dp/dz$) nearly matches the buoyancy term (ρg). But, the difference, $-dp/dz - \rho g$, is equal to the nonlinear term that leads to Reynolds number $Re \propto Ra^{1/2}$.

Keywords: Compressible thermal convection, Turbulent thermal convection, Solar convection

1. Introduction

Turbulent thermal convection occurs in a wide range of geophysical and astrophysical flows, as well as in many natural and industrial processes [1, 2, 3, 4, 5, 6, 7, 8]. There are various models of turbulent convection, the leading one being Rayleigh-Bénard convection (RBC) [1, 2, 3, 4, 5] that follows Oberbeck-Boussinesq (OB) approximation. In RBC, a horizontal layer of fluid confined between two parallel plates is heated from below and cooled from above. In the OB approximation, the density of the fluid is nearly constant, except for a small variation in the buoyancy term. For example, for water, whose thermal expansion coefficient $\alpha \approx 3 \times 10^{-4} \text{ K}^{-1}$ at room temperature, the relative change in density $(\delta\rho)/\rho \approx \alpha(\Delta T) \approx 10^{-3}$ when the temperature difference between the two plates is around 30 K [5].

However, $(\delta\rho)/\rho$ in a turbulent star is of the order of unity [9]. Let us assume that the star is made of ideal gas, whose thermal expansion coefficient is $1/T$, where T is the gas temperature. Hence, $(\delta\rho)/\rho \approx \alpha(\Delta T) \approx 1$ when $(\Delta T) \approx T$. Therefore, the OB approximation and the RBC equations become invalid for stars and related

astrophysical systems [6, 10, 11, 12]. To study such systems, researchers often employ equations for compressible convection or intermediate models that employ non-Oberbeck-Boussinesq (NOB) effects [13, 14, 15] or anelastic approximations [16, 17]. In this paper, we employ fully compressible equations to study turbulent convection at very large Rayleigh numbers (Ra)—up to 10^{15} for two-dimensions (2D), and 10^{11} for three-dimension (3D). Note, however, that the solar convection has even larger Ra ($\sim 10^{24}$) than the above [6].

Many aspects of turbulent convection, which is more complex than hydrodynamic turbulence, are understood quite well, in particular for RBC systems. Grossmann and Lohse (GL in short) [18, 19] modelled the Reynolds number (Re) and Nusselt number (Nu) scaling using the relations for viscous and thermal dissipation rates [20, 21]. The GL relations have been verified by many experiments and numerical simulations [22]. Recently, Bhattacharya and Verma [23] employed machine learning, artificial intelligence, and more accurate dissipation rates for Ra and Pr predictions. In addition, it has been shown that for small and moderate Prandtl numbers ($Pr \lesssim 1$), turbulent convection has properties similar to hydrodynamic turbulence [5, 24]. For example, the energy spectrum for turbulent convection follows Kolmogorov's $5/3$ spectrum.

For the RBC setup, while the Reynolds number scaling is reasonably well established, the properties of velocity fluctuations remains to be quantified [25]. Addi-

*Corresponding author

¹tharshit@iitk.ac.in

²lekhasharma27@gmail.com

³mkv@iitk.ac.in

tionally, accurate characterization of the Nusselt number scaling remains a challenge. Two main theories describe the dependence of Nu on Ra. In the extreme turbulent regime, known as *ultimate regime*, Kraichnan argued that Nu scales as $Ra^{1/2}$ [26, 27]. On the contrary, Malkus [28] proposed that Nu is proportional to $Ra^{1/3}$, referred to as the *classical scaling* [1, 2, 3, 4, 18, 27]. It is reported both in experiments and numerical simulations that up to $Ra = 10^{12}$, the Nu scaling exponent is near 0.30. However, Chavanne et al. [29], He et al. [30], Zhu et al. [31] and some others argued that the Nu exponent gradually increases to about 0.38 near $Ra = 10^{15}$. Therefore, some researchers believe that the exponent might reach the value 1/2 at extreme Ra's [27]. But, some others, based on different experiments and related simulations, argue that the classical scaling will remain valid for all Ra's [6, 32, 33, 34]. The scaling of Nu is discussed in detail in recent articles [27, 35].

Turbulent compressible convection behaves very differently than RBC turbulence [36]. Unlike the constant bulk temperature in RBC, the bulk temperature in compressible convection falls adiabatically [17]. In compressible convection, the fluid at the bottom is heavier than that at the top, which is in sharp contrast to that in RBC. Unfortunately, compressible convection has not been studied extensively. In recent times, Verhoeven et al. [17], and John and Schumacher [36, 37, 38] analyzed turbulent compressible convection. Verhoeven et al. [17] performed a comparative study of the anelastic approximation and fully compressible turbulent convection. John and Schumacher [36, 37] performed numerical simulations of fully compressible convection up to $Ra = 10^7$ and explored different regimes of compressible convection. Some compressible simulations use inviscid flows [39] whose Ra estimates are somewhat uncertain. We find that there are no existing studies on fully compressible convection at very high Rayleigh numbers. The present paper aims to fill this gap.

In this paper, we simulate turbulent compressible convection using a computationally-efficient MacCormack-TVD (total variation diminishing) finite difference method that eliminates numerical oscillations [40]. Our method is an extension of the novel and stable numerical scheme proposed by Ouyang et al. [40], Yee [41], and Liang et al. [42] for shallow water equations to compressible turbulent convection. Our stable numerical scheme enabled us to perform convection simulations at very large Ra's, e.g., 10^{15} for 2D flows, and 10^{11} for 3D flows.

We quantify various quantities using the data generated by our numerical simulations. Our numerical data show that the internal energy dominates the fluid kinetic

energy even at very large Ra. We attribute adiabaticity to this effect. In addition, we study the superadiabatic temperature and density of the flow. Based on numerical data, we report that $Nu \sim Ra^{0.3}$ up to $Ra = 10^{15}$ in 2D and up to 10^{11} in 3D. We caution that our results differ significantly from those for RBC, which is very different from compressible convection. Among the two, compressible equations model the astrophysical systems better.

Simulations of 3D turbulent convection at extreme Ra's are very expensive. Fortunately, in the RBC framework, the scaling of Nu and Re for 2D and 3D flows are reasonably similar for $Pr \gtrsim 1$ [43, 44, 45]. Motivated by these observations, we examine the Nu and Re scaling for extreme Ra in 2D, and for moderate Ra in 3D. We believe that these important findings will improve the models of stellar and planetary convection.

We have organised the paper as follows. In Sec. 2, we describe the physical system along with the governing equations. Sec. 3 discusses the numerical scheme along with the simulation parameters. In Secs. 4 and 5, we describe the adiabaticity and boundary layers in turbulent convection. Section 6 contains discussions on Nu and Re scaling. We conclude in Sec. 7.

2. Physical System and Governing Equations

We consider a fully compressible fluid confined in a rectangular box of dimension (L, L, d) in 3D and (L, d) in 2D, with the bottom and top plates at temperatures T_b and T_t respectively ($T_b > T_t$). Note that the adverse temperature gradient $\Delta = (T_b - T_t)/d > 0$. We employ periodic boundary condition for the vertical sideways walls. However, for the top and bottom plates, we employ no-slip boundary conditions for the velocity field, and conducting boundary conditions for the temperature field [17, 37]. Note that a perfectly conducting plate maintains constant temperatures throughout its volume.

We assume that the fluid has constant dynamic viscosity μ and thermal conductivity K . We also assume that the fluid follows ideal gas law, $\tilde{p} = \tilde{\rho}R_*\tilde{T}$, where \tilde{p} is the pressure; $\tilde{\rho}$ is the density of fluid; $R_* = C_p - C_v$ is the gas constant; C_p, C_v are the specific heat capacities at constant pressure and volume respectively; and \tilde{T} is the temperature field. The following conservative set of equations govern the system [9, 46]:

$$\frac{\partial \tilde{p}}{\partial \tilde{t}} + \frac{\partial}{\partial \tilde{x}_i}(\tilde{\rho}\tilde{u}_i) = 0, \quad (1)$$

$$\frac{\partial}{\partial \tilde{t}}(\tilde{\rho}\tilde{u}_i) + \frac{\partial}{\partial \tilde{x}_j}(\tilde{\rho}\tilde{u}_i\tilde{u}_j + \delta_{ij}\tilde{p} - \tilde{\tau}_{ij}) = -g\tilde{\rho}\delta_{iz}, \quad (2)$$

Nomenclature

d	height of rectangular box	\tilde{H}_T	dimensional total heat flux
L	length and width of rectangular box	\tilde{H}_A	dimensional adiabatic heat flux
g	gravitational acceleration	\tilde{H}_{cond}	dimensional conductive heat flux
K	thermal conductivity	\tilde{H}_{conv}	dimensional convective heat flux
T_b	temperature at the bottom plate	$\overline{\text{Nu}}$	mean Nusselt number
T_t	temperature at the top plate	Nu	bulk Nusselt number
C_p	specific heat capacity at constant pressure	Nu_{conv}	convective Nusselt number
C_v	specific heat capacity at constant volume	Nu_K	u_z -induced kinetic Nusselt number
R_*	gas constant	\tilde{U}	dimensional root-mean square velocity
$\tilde{\mathbf{r}} = (\tilde{x}, \tilde{y}, \tilde{z})$	dimensional position vector	U	nondimensional root-mean square velocity
$\mathbf{r} = (x, y, z)$	nondimensional position vector	\mathbf{X}	column vector containing ρ , ρu_α , and E
$\tilde{\mathbf{u}}$	dimensional velocity	\mathbf{F}_α	fluxes in α -direction
\mathbf{u}	nondimensional velocity	\mathbf{S}_α	sources in α -direction
\tilde{t}	dimensional time	\mathbf{L}_α	predictor-corrector operator α -direction
t	nondimensional time	Co_α	local Courant number in α -direction
\tilde{T}	dimensional temperature	$C(\text{Ra})$	correlation between ρu_z and T_{sa}
T	nondimensional temperature		
\tilde{p}	dimensional pressure	<i>Greek:</i>	
p	nondimensional pressure	Γ	aspect ratio of computational domain
\tilde{E}	dimensional total energy density	Δ	temperature gradient in z -direction
E	nondimensional total energy density	γ	ratio of specific heats
\tilde{T}_A	dimensional adiabatic temperature	μ	dynamic viscosity
T_A	nondimensional adiabatic temperature	ν	kinematic viscosity
\tilde{p}_A	dimensional adiabatic pressure	κ	thermal diffusivity
p_A	nondimensional adiabatic pressure	$\tilde{\rho}$	dimensional fluid density
\tilde{T}_{sa}	dimensional superadiabatic temperature	ρ	nondimensional fluid density
T_{sa}	nondimensional superadiabatic temperature	$\tilde{\rho}_A$	dimensional adiabatic density field
Pr	Prandtl number	ρ_A	nondimensional adiabatic density field
Ra	Rayleigh number	β	adiabatic index
Re	Reynolds number	ϵ	superadiabaticity
D	dissipation number	$\tilde{\boldsymbol{\tau}}$	dimensional stress tensor
$r = K_e/I_e$	ratio of kinetic energy and internal energy	$\boldsymbol{\tau}$	nondimensional stress tensor

$$\frac{\partial \tilde{E}}{\partial \tilde{t}} + \frac{\partial}{\partial \tilde{x}_i} \left(\tilde{u}_i (\tilde{E} + \tilde{p}) - K \frac{\partial \tilde{T}}{\partial \tilde{x}_i} - \tilde{u}_j \tilde{\tau}_{ij} \right) = 0, \quad (3)$$

where \tilde{u}_i are the velocity field components; g is the acceleration due to gravity along $-\hat{z}$ direction;

$$\tilde{E} = \tilde{\rho} \left(\frac{\tilde{u}^2}{2} + C_v \tilde{T} + g \tilde{z} \right) \quad (4)$$

is the total energy density; and

$$\tilde{\tau}_{ij} = \mu \left(\tilde{\partial}_j \tilde{u}_i + \tilde{\partial}_i \tilde{u}_j + \frac{2}{3} \tilde{\partial}_m \tilde{u}_m \delta_{ij} \right) \quad (5)$$

is the stress tensor. Another important parameter is the aspect ratio Γ , which is the ratio of the length (L) and

the height (d) of the rectangular box. All tilde variables have their respective dimensions.

The bulk flow is nearly adiabatic (or isentropic) because the convection time scale is faster than the conduction time scale (estimates in Sec. 4). Therefore, the vertical profiles of the adiabatic temperature $\tilde{T}_A(\tilde{z})$, adiabatic density $\tilde{\rho}_A(\tilde{z})$, and adiabatic pressure $\tilde{p}_A(\tilde{z})$ are [9, 17]

$$\tilde{T}_A(\tilde{z}) = \left(T_b - \frac{g}{C_p} \tilde{z} \right), \quad (6)$$

$$\tilde{\rho}_A(\tilde{z}) = \frac{\rho_b}{T_b^\beta} (\tilde{T}_A(\tilde{z}))^\beta, \quad (7)$$

$$\tilde{p}_A(\tilde{z}) = (C_p - C_v) \tilde{\rho}_A(\tilde{z}) \tilde{T}_A(\tilde{z}), \quad (8)$$

where T_b and ρ_b are respectively the temperature and fluid density at the bottom plate; and $\beta = 1/(\gamma - 1)$ is the adiabatic index with $\gamma = C_p/C_v$. Later in the paper we will show the bulk temperature nearly follows the adiabatic profile [Eq. (6)]. The difference between the real temperature and the adiabatic profile is called *superadiabatic temperature*: $\tilde{T}_{sa}(\tilde{\mathbf{r}}, \tilde{t}) = \tilde{T}(\tilde{\mathbf{r}}, \tilde{t}) - \tilde{T}_A(\tilde{z})$.

Compressible convection has several important nondimensional parameters, which are [17, 36]

$$\text{superadiabaticity } \epsilon = \frac{d}{T_b} \left(\frac{\Delta}{d} - \frac{g}{C_p} \right), \quad (9)$$

$$\text{dissipation number } D = \frac{gd}{T_b C_p} = \frac{T_b - \tilde{T}_A(d)}{T_b}, \quad (10)$$

$$\text{Rayleigh number } \text{Ra} = \frac{\epsilon g d^3}{\nu \kappa}, \quad (11)$$

$$\text{Prandtl number } \text{Pr} = \frac{\nu}{\kappa}, \quad (12)$$

where $\nu = \mu/\rho$ is the kinematic viscosity, and $\kappa = K/(C_p \rho)$ is the thermal diffusivity of fluid. The parameters Ra and Pr are common with RBC, except that the temperature gradient has an adiabatic correction via ϵ . The parameters D and ϵ are unique to compressible convection: D represents the nondimensional adiabatic temperature drop, whereas ϵ represents the excess temperature gradient relative to the adiabatic profile [17, 36]. In Fig. 1(A,B), we plot the total temperature gradient and the adiabatic temperature gradient in dimensional and nondimensional forms respectively.

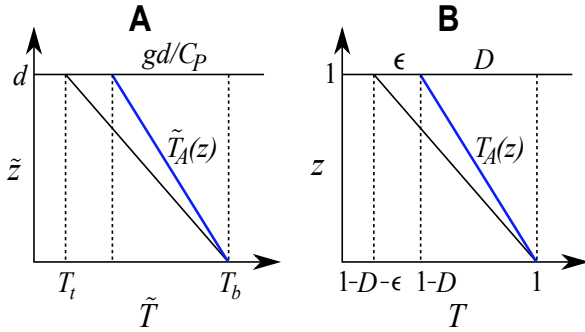


Figure 1: The adiabatic temperature gradient (blue lines) and the total temperature gradients (black lines) in (A) dimensional and (B) non-dimensional forms.

In Sec. 4, we will show that the bulk temperature nearly follows the adiabatic temperature profile $\tilde{T}_A(\tilde{z})$, which is in sharp contrast to RBC where the bulk temperature is constant. Additionally, the density at the bottom is larger than that at the top, which is opposite to that in RBC. Therefore, compressible convection exhibits behavior that is markedly different from that of

RBC.

We non-dimensionalize Eqs. (1)-(3) using d as the length scale, free-fall velocity $\sqrt{\epsilon g d}$ as the velocity scale, ρ_b as the density scale, and T_b as the temperature scale. The governing equations in dimensionless form are [17, 37]

$$\frac{\partial \rho}{\partial t} + \frac{\partial}{\partial x_i} (\rho u_i) = 0, \quad (13)$$

$$\frac{\partial}{\partial t} (\rho u_i) + \frac{\partial}{\partial x_j} (\rho u_i u_j + \delta_{ij} p - \tau_{ij}) = -\frac{1}{\epsilon} \rho \delta_{iz}, \quad (14)$$

$$\frac{\partial E}{\partial t} + \frac{\partial}{\partial x_i} \left(u_i (E + p) - \frac{1}{\epsilon D \sqrt{\text{RaPr}}} \frac{\partial T}{\partial x_i} - u_j \tau_{ij} \right) = 0, \quad (15)$$

where the nondimensionalized pressure, total energy density, and stress tensor are defined respectively as:

$$p = \frac{(\gamma - 1)}{\gamma \epsilon D} \rho T, \quad (16)$$

$$E = \rho \left(\frac{u^2}{2} + \frac{1}{\gamma \epsilon D} T + \frac{1}{\epsilon} z \right), \quad (17)$$

$$\tau_{ij} = \sqrt{\frac{\text{Pr}}{\text{Ra}}} \left(\partial_j u_i + \partial_i u_j + \frac{2}{3} \partial_m u_m \delta_{ij} \right). \quad (18)$$

Note that the tilde variables are dimensional, whereas those without tilde are dimensionless. The nondimensional adiabatic profiles are [17]

$$T_A(z) = (1 - Dz), \quad (19)$$

$$\rho_A(z) = (1 - Dz)^\beta, \quad (20)$$

$$p_A(z) = (1 - Dz)^{(\beta+1)}. \quad (21)$$

The nondimensional temperature is 1 at the bottom plate, and $1 - \epsilon - D$ at the top plate (see Fig. 1).

In this paper, we study heat transport as a function of Ra for a fixed Pr, ϵ , and D . In the RBC framework, Nu is the ratio of total heat flux (\tilde{H}_T) and conductive heat flux (\tilde{H}_{cond}). In compressible convection, the heat flux due to adiabatic cooling (\tilde{H}_A) must be subtracted from both \tilde{H}_T and \tilde{H}_{cond} to compensate the thermodynamic effects [11, 46, 47]. Here, the total heat flux is a sum of $\tilde{H}_{\text{cond}} = K \Delta$ (K is the thermal conductivity of the fluid), convective heat flux $\tilde{H}_{\text{conv}} = C_p \langle \tilde{\rho} \tilde{u}_z \tilde{T}_{sa} \rangle_{V,t}$, and u_z -induced kinetic heat flux $\tilde{H}_K = \langle \tilde{\rho} \tilde{u}_z \tilde{u}^2 / 2 \rangle_{V,t}$. The adiabatic heat flux is given by $\tilde{H}_A = K g / C_p$. Hence, the

Nusselt number is [46, 47]

$$\begin{aligned} \text{Nu} &= \frac{\tilde{H}_T - \tilde{H}_A}{\tilde{H}_{\text{cond}} - \tilde{H}_A} \\ &= \frac{K\Delta + C_p \langle \tilde{\rho} \tilde{u}_z \tilde{T}_{\text{sa}} \rangle_{V,t} + \langle \tilde{\rho} \tilde{u}_z \tilde{u}^2 / 2 \rangle_{V,t} - Kg/C_p}{K \left(\Delta - \frac{g}{C_p} \right)} \\ &= 1 + \frac{\sqrt{\text{RaPr}}}{\epsilon} \langle \rho u_z T_{\text{sa}} \rangle_{V,t} + \frac{D \sqrt{\text{RaPr}}}{2} \langle \rho u_z u^2 \rangle_{V,t} \\ &= 1 + \text{Nu}_{\text{conv}} + \text{Nu}_K. \end{aligned} \quad (22)$$

We report the volume and temporal averages of the above quantities and denote them by $\langle \cdot \rangle_{V,t}$.

The above Nu, called *bulk Nusselt number*, fluctuates significantly. In contrast, the Nusselt number computed near the bottom plate ($z = 0$) and top plate ($z = 1$) [17, 37]

$$\text{Nu}_{z=0,1} = -\frac{1}{\epsilon} \left. \frac{d \langle T_{\text{sa}} \rangle_{A,t}}{dz} \right|_{z=0,1}, \quad (23)$$

have much less fluctuations. Here $\langle \cdot \rangle_{A,t}$ represents the horizontal and temporal averages. Consequently, the mean Nusselt number at the boundaries is given by

$$\overline{\text{Nu}} = \frac{\text{Nu}_{z=0} + \text{Nu}_{z=1}}{2}. \quad (24)$$

In this paper, we report Nu and $\overline{\text{Nu}}$, as well as Nu_{conv} and Nu_K . In addition to Nu, we also report the Reynolds number Re, which is defined as [5]

$$\text{Re} = \frac{\tilde{U}d}{\nu}, \quad (25)$$

where \tilde{U} is the root-mean-square (rms) velocity. After non-dimensionalization [17],

$$\text{Re} = \sqrt{\frac{\text{Ra}}{\text{Pr}}} U = \sqrt{\frac{\text{Ra}}{\text{Pr}}} \langle \sqrt{\langle u^2 \rangle_V} \rangle_t. \quad (26)$$

where U is the dimensionless velocity.

In Sec. 3, we solve Eqs. (13)-(15) numerically.

3. Numerical Method, Validation, and Simulation Parameters

In this section, we describe our numerical method, its validation, and the simulation parameters.

3.1. Numerical Method

We solve Eqs. (13)-(15) using MacCormack-TVD (total variation diminishing) finite-difference scheme on a collocated grid [40, 41, 42]. We employ a non-uniform tangent-hyperbolic grid in the z -direction to increase

resolution near the boundaries, and uniform grids along the x and y directions.

All the equations are written in vectorial notation in the following conservative form [40]:

$$\frac{\partial \mathbf{X}}{\partial t} + \sum_{\alpha} \frac{\partial \mathbf{F}_{\alpha}}{\partial x_{\alpha}} = \sum_{\alpha} \mathbf{S}_{\alpha}, \quad (27)$$

where $\alpha = 1, 2, 3$ represent the $x, y,$ and z directions respectively. \mathbf{X} is a column vector that contains the variables $\rho, \rho u_{\alpha}$, and E ; \mathbf{F}_{α} and \mathbf{S}_{α} are the respective fluxes and sources [48]. Hence,

$$\mathbf{X} = \begin{bmatrix} \rho \\ \rho u_x \\ \rho u_y \\ \rho u_z \\ E \end{bmatrix}; \quad \mathbf{S}_1 = \begin{bmatrix} 0 \\ f_1 \\ 0 \\ 0 \\ 0 \end{bmatrix}; \quad \mathbf{S}_2 = \begin{bmatrix} 0 \\ 0 \\ f_2 \\ 0 \\ 0 \end{bmatrix}; \quad \mathbf{S}_3 = \begin{bmatrix} 0 \\ 0 \\ 0 \\ f_3 \\ 0 \end{bmatrix};$$

$$\mathbf{F}_{\alpha} = \begin{bmatrix} \rho u_{\alpha} \\ \rho u_x u_{\alpha} - \tau_{x\alpha} \\ \rho u_y u_{\alpha} - \tau_{y\alpha} \\ \rho u_z u_{\alpha} - \tau_{z\alpha} + p \\ u_{\alpha}(E + p) - K \frac{\partial T}{\partial x_{\alpha}} - \sum_{\beta} u_{\beta} \tau_{\beta\alpha} \end{bmatrix}. \quad (28)$$

For natural convection, $f_1 = 0, f_2 = 0,$ and $f_3 = -\rho g$. Using operator-splitting method, we separate the Eq. (27) into three one-dimensional equations:

$$\frac{\partial \mathbf{X}}{\partial t} + \frac{\partial \mathbf{F}_1}{\partial x_1} = \mathbf{S}_1, \quad \frac{\partial \mathbf{X}}{\partial t} + \frac{\partial \mathbf{F}_2}{\partial x_2} = \mathbf{S}_2, \quad \frac{\partial \mathbf{X}}{\partial t} + \frac{\partial \mathbf{F}_3}{\partial x_3} = \mathbf{S}_3. \quad (29)$$

The fields in \mathbf{X} are discretized in space, whose value at the site (i, j, k) is \mathbf{X}_{ijk} . We denote the time step using superscript (n) . The time stepping of \mathbf{X}_{ijk} from (n) to $(n+1)$ is [40]

$$\begin{aligned} \mathbf{X}_{ijk}^{(n+1)} &= \mathbf{L}_x \left(\frac{\delta t}{2} \right) \mathbf{L}_y \left(\frac{\delta t}{2} \right) \mathbf{L}_z \left(\frac{\delta t}{2} \right) \times \\ &\quad \mathbf{L}_x \left(\frac{\delta t}{2} \right) \mathbf{L}_y \left(\frac{\delta t}{2} \right) \mathbf{L}_z \left(\frac{\delta t}{2} \right) \mathbf{X}_{ijk}^{(n)}, \end{aligned} \quad (30)$$

where δt is the time-step; and \mathbf{L}_{α} is predictor-corrector operator in α -direction. The last three terms of Eq. (30) carry forward \mathbf{X} from (n) to $(n+1/2)$, whereas the first three terms take from $(n+1/2)$ to $(n+1)$, each of which involves several sub-steps.

Along the z -direction ($\alpha = 3$), a predictor step from (n) to $(n+1/2)$ using backward difference is [40]

$$\mathbf{X}_{ijk}^P = \mathbf{X}_{ijk}^{(n)} - \frac{\delta t}{2} \left(\frac{\mathbf{F}_{\alpha,ijk}^{(n)} - \mathbf{F}_{\alpha,ijk(k-1)}^{(n)}}{\delta x_{\alpha}} \right) + \frac{\delta t}{2} \mathbf{S}_{\alpha,ijk}^{(n)}. \quad (31)$$

After this step, we perform the corrector step [40]

$$\mathbf{X}_{ijk}^C = \mathbf{X}_{ijk}^{(n)} - \frac{\delta t}{2} \left(\frac{\mathbf{F}_{\alpha,ijk(k+1)}^{(n)} - \mathbf{F}_{ijk}^P}{\delta x_{\alpha}} \right) + \frac{\delta t}{2} \mathbf{S}_{\alpha,ijk}^P. \quad (32)$$

We take an average of the above steps and add the TVD correction term $\mathbf{T}_{ijk}^{(n+1/2)}$, which yields [40]

$$\mathbf{X}_{ijk}^{(n+1/2)} = \frac{\mathbf{X}_{ijk}^P + \mathbf{X}_{ijk}^C}{2} + \mathbf{T}_{ijk}^{n+1/2}, \quad (33)$$

where

$$\mathbf{T}_{ijk}^{n+1/2} = \frac{G(r_{ijk}^+ + r_{ij(k+1)}^-) \delta \mathbf{X}_{ij(k+1/2)}^n - G(r_{ij(k-1)}^+ + r_{ijk}^-) \delta \mathbf{X}_{ij(k-1/2)}^n}{2}, \quad (34)$$

$$\delta \mathbf{X}_{ij(k+1/2)}^n = \mathbf{X}_{ij(k+1)}^n - \mathbf{X}_{ijk}^n, \quad (35)$$

$$\delta \mathbf{X}_{ij(k-1/2)}^n = \mathbf{X}_{ijk}^n - \mathbf{X}_{ij(k-1)}^n, \quad (36)$$

$$r_{ijk}^\pm = \frac{(\delta \mathbf{X}_{ij(k-1/2)}^n, \delta \mathbf{X}_{ij(k+1/2)}^n)}{(\delta \mathbf{X}_{ij(k\pm 1/2)}^n, \delta \mathbf{X}_{ij(k\pm 1/2)}^n)}. \quad (37)$$

The bracket (\mathbf{A}, \mathbf{B}) indicates the dot product between \mathbf{A} and \mathbf{B} , and

$$G(x) = 0.5C(1 - \phi(x)), \quad (38)$$

where $\phi(x) = \max(0, \min(2x, 1))$ is the *minmod flux limiter function*, and

$$C = \begin{cases} \text{Co}_\alpha(1 - \text{Co}_\alpha), & \text{Co}_\alpha \leq 0.5 \\ 0.25, & \text{Co}_\alpha > 0.5 \end{cases} \quad (39)$$

with Co_α representing the local Courant number in α -direction [40, 41]. Identical processes are also adopted for the x - and y -directions.

The TVD correction preserves monotonicity and prevents spurious oscillations in the solution [41]. The MacCormack-TVD scheme is second-order accurate in space and time. For computing the boundary points, we use second-order forward and backward differences at the bottom and top plates, respectively.

3.2. Programming Tools

We developed an object-oriented Python solver, DHARA, for simulating fully compressible equations on many GPUs and CPUs. The solver employs CuPy library [49] for GPU acceleration, and mpi4py [50] for multi-GPU communications. Note that CuPy provides a GPU-optimized alternative to NumPy [51]. We enhanced the code performance using `cupy.ElementwiseKernel()`, leading to 200X speedup on NVIDIA A100 GPU in comparison to a single-core AMD EPYC 7543 processor. For scaling studies, we ran DHARA on 128 nodes (512 A100 GPUs) of Polaris (Argonne National Laboratory) and

on 1024 nodes (8192 AMD MI250X GPUs) of Frontier (Oak Ridge National Laboratory) and demonstrated near ideal scaling (see Appendix A).

We performed the majority of our convection simulations on Polaris. Some simulations with smaller grids were performed on the Param Sanganak supercomputer of IIT Kanpur and on our laboratory clusters.

3.3. Validation

We validate our code by comparing our numerical Nusselt and Reynolds numbers with those computed by John and Schumacher [37] and Verhoeven et al. [17]. We compute Nu using Eq. (24). In particular, we simulate Eqs. (13)-(15) for $\text{Ra} = 10^6$, $\epsilon = 0.1$, $\Gamma = 4$, $\gamma = 1.4$, $\text{Pr} = 0.7$, and $D = 0.1, 0.34, 0.5, 0.6$. The Nu and Re computed by our code and those by John and Schumacher [37] are listed in Table 1. Next, we compute Re and Nu by varying Ra for a fixed $D = 0.49$, $\Gamma = 2$, $\gamma = \frac{5}{3}$, $\epsilon = 0.1$, $\text{Pr} = 0.7$, and compare our results with Verhoeven et al. [17] (see Table 2). Our results show good agreement with those reported by John and Schumacher [37] and Verhoeven et al. [17]. Our Nu and Re differ from the previous works by less than 3%.

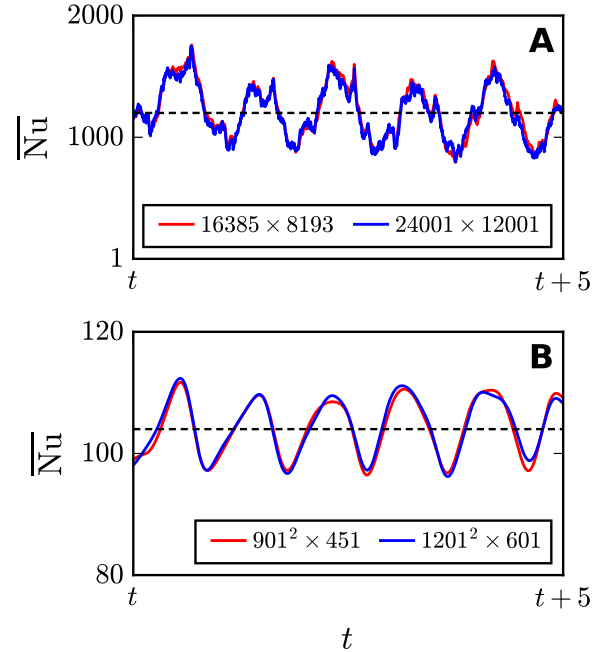


Figure 2: For $\epsilon = 0.1, D = 0.5, \gamma = 1.3, \Gamma = 4$, and $\text{Pr} = 0.7$, the time series of $\overline{\text{Nu}}$ computed using Eq. (24) for (A) 2D convection at $\text{Ra} = 10^{15}$ on grids 16385×8193 (red) and 24001×12001 (blue), and for (B) 3D convection at $\text{Ra} = 10^{11}$ on grids $901^2 \times 451$ (red) and $1201^2 \times 601$ (blue).

Table 1: Comparison between our Nu and Re and those of John and Schumacher [37] for $Ra = 10^6$, $Pr = 0.7$, $\Gamma = 4$, $\gamma = 1.4$, $\epsilon = 0.1$, and various D 's.

Case	D	Nu [37]	Nu (our simulations)	Error _{Nu} (in %)	Re [37]	Re (our simulations)	Error _{Re} (in %)
1	0.1	7.94	7.90 ± 0.06	0.7	424	425 ± 3	0.7
2	0.34	7.64	7.67 ± 0.08	1.0	414	414 ± 4	0.9
3	0.5	6.93	6.89 ± 0.05	0.7	407	406 ± 3	0.7
4	0.6	6.24	6.18 ± 0.09	1.4	370	368 ± 5	1.3

Table 2: Comparison between our Nu and Re and those of Verhoeven et al. [17] for $D = 0.49$, $\epsilon = 0.1$, $Pr = 0.7$, $\Gamma = 2$, $\gamma = \frac{5}{3}$, and various Ra 's.

Case	Ra	Nu [17]	Nu (our simulations)	Error _{Nu} (in %)	Re [17]	Re (our simulations)	Error _{Re} (in %)
1	10^4	2.1	2.175 ± 0.005	0.2	26.3	26.98 ± 0.05	0.2
2	10^5	3.9	4.0 ± 0.1	2.5	102	100 ± 3	3.3
3	10^6	7.1	7.3 ± 0.2	2.7	322	330 ± 7	2.0
4	10^7	13.4	14.1 ± 0.4	2.8	973	970 ± 20	2.4

We also perform grid independence test by comparing Nu for 2D convection at $Ra = 10^{15}$ on grids 16385×8193 and 24001×12001 , and for 3D convection at $Ra = 10^{11}$ on grids $901^2 \times 451$ and $1201^2 \times 601$. We compute \overline{Nu} for the steady states using Eq. (24) and plot the time series in Fig. 2(A, B) for 2D and 3D, respectively. The respective \overline{Nu} for 2D at $Ra = 10^{15}$ are 1218 and 1204, and for 3D at $Ra = 10^{11}$ are 103 and 104, which are within 1% of each other. The near similarity of Nu time series and their averages indicate that our results are grid independent, as long as the flow is well resolved.

3.4. Simulation Parameters

We simulate Eqs. (13)-(15) in 2D and 3D using the numerical scheme described in Sec. 3.1. For the horizontal plates, we employ no-slip boundary condition for the velocity field and conducting boundary condition for the temperature field. The fields at the side walls satisfy periodic boundary condition.

For our simulations, we fix $\Gamma = 4$, $\gamma = 1.3$, $\epsilon = 0.1$, $D = 0.5$, $Pr = 0.7$ and vary Ra . The Rayleigh number Ra ranges from 10^9 to 10^{15} for 2D, and from 10^8 to 10^{11} for 3D. In Table 3, we list the grid sizes, Ra , \overline{Nu} , Re, number of points in the top and bottom boundary layers (N_t^{BL} and N_b^{BL} respectively), and thicknesses of the top and bottom boundary layers (λ_t and λ_b respectively).

We compute \overline{Nu} and Re using Eqs. (24, 26) respectively. However, \overline{Nu} and Re exhibit significant fluctuations, hence we average them over 50 time units in the steady state, except that we average over 30 and 20 time units for $Ra = 10^{14}$ and 10^{15} respectively. We list these values in Table 3. Note that \overline{Nu} has around 10% errors for the 2D runs, but has maximum of 4% error for the

3D runs. The errors in Re range from 1% to 15% for 2D flows, and from 0.5% to 2% for 3D flows.

The highest grid resolutions are 16385×8193 for 2D, and $901^2 \times 451$ for 3D. For all our runs, the number of grid points in the boundary layers exceeds 5, hence they satisfy the Grötzbach resolution criteria [27, 52, 53, 54]. These observations indicate that our simulations are well resolved. For faster execution, we employ a single or multiple GPUs: a single GPU for Runs 1-5 and 8; and 4 GPUs for Runs 6, 7 and 9-11 of Table 3. Our largest 3D run with $901^2 \times 451$ grid required 7 days to complete on a Polaris node with four NVIDIA A100 GPUs.

In the following three sections, we will discuss various properties of compressible convection. We start with adiabatic profile and flow structures of the flow.

4. Adiabatic Profile and Flow Structures

According to *Schwarzschild criterion*, at the onset of convection, the temperature in compressible convection decreases vertically with the rate g/C_p , which is the adiabatic temperature profile [55]. This result is derived using equilibrium thermodynamics. Interestingly, the atmospheres of the Earth and Sun too exhibit adiabatic temperature drop even though these systems are turbulent [6]. As we show below, we observe adiabatic cooling in our high Ra simulations, consistent with solar and Earth convection.

Table 3: For our 2D convection Runs 1 to 7, and 3D Runs 8 to 11: the Rayleigh number Ra , the grid size, the Reynolds number Re , the mean Nusselt number \overline{Nu} , the number of grid points in the top and bottom boundary layers (N_t^{BL} , N_b^{BL}), and the thicknesses of top and bottom thermal boundary layers (λ_t , λ_b). Also, the polytropic index $\gamma = 1.3$, Prandtl number $Pr = 0.7$, dissipation number $D = 0.5$, superadiabaticity $\epsilon = 0.1$, and the aspect ratio $\Gamma = 4$.

Run	Ra	Grid Size	Re	\overline{Nu}	N_t^{BL}	N_b^{BL}	λ_t	λ_b
1	10^9	3001×1501	$(1.35 \pm 0.01) \times 10^4$	22 ± 3	133	34	0.055	0.013
2	10^{10}	5001×2501	$(4.23 \pm 0.01) \times 10^4$	42 ± 5	180	54	0.036	0.010
3	10^{11}	5601×2801	$(1.28 \pm 0.03) \times 10^5$	90 ± 10	120	38	0.020	0.0062
4	10^{12}	6001×3001	$(4.04 \pm 0.07) \times 10^5$	180 ± 20	95	32	0.015	0.0047
5	10^{13}	8193×4097	$(1.3 \pm 0.1) \times 10^6$	360 ± 50	70	23	0.010	0.0031
6	10^{14}	12001×6001	$(4.0 \pm 0.2) \times 10^6$	570 ± 70	72	21	0.0066	0.002
7	10^{15}	16385×8193	$(1.3 \pm 0.2) \times 10^7$	1200 ± 200	62	18	0.0042	0.0012
8	10^8	$513^2 \times 257$	$(2.21 \pm 0.01) \times 10^3$	14.0 ± 0.2	35	12	0.076	0.0226
9	10^9	$801^2 \times 401$	$(6.86 \pm 0.02) \times 10^3$	28.6 ± 0.5	32	11	0.047	0.0158
10	10^{10}	$801^2 \times 401$	$(2.03 \pm 0.04) \times 10^4$	53.9 ± 0.5	20	7	0.028	0.010
11	10^{11}	$901^2 \times 451$	$(5.86 \pm 0.08) \times 10^4$	103 ± 4	13	5	0.017	0.0061

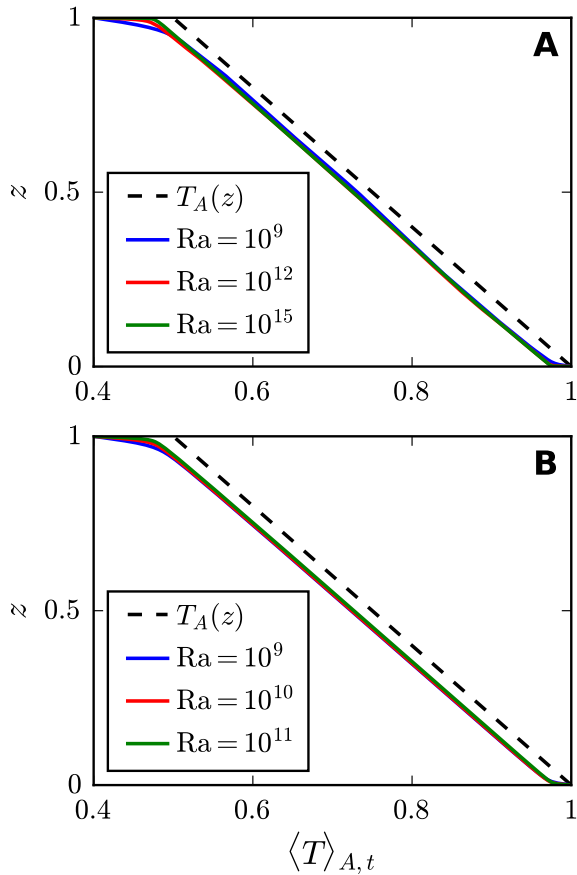


Figure 3: Profiles of horizontally and temporally averaged $\langle T \rangle_{A,t}(z)$ for (A) 2D convection for $Ra = 10^9$ (blue), $Ra = 10^{12}$ (red), and $Ra = 10^{15}$ (green); and (B) 3D convection for $Ra = 10^9$ (blue), $Ra = 10^{10}$ (red), and $Ra = 10^{11}$ (green). The black dashed line represents the adiabatic temperature ($T_A(z)$).

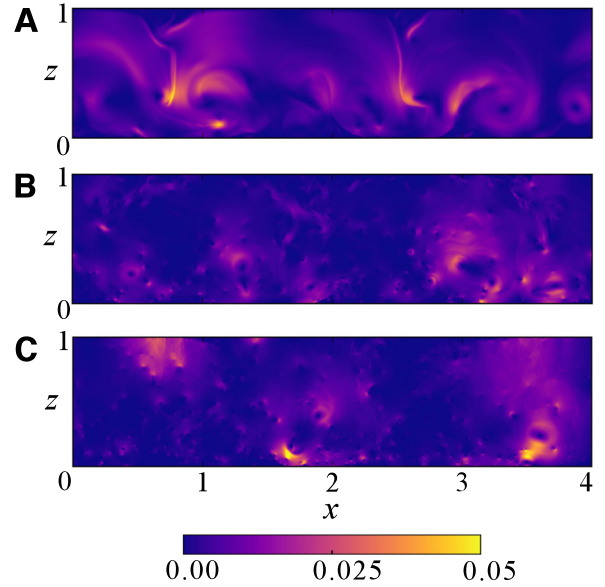


Figure 4: For 2D compressible convection with (A) $Ra = 10^9$, (B) 10^{12} , and (C) 10^{15} , the density plots of the ratio of fluid kinetic energy and internal energy, $r = (\rho u^2/2)/(\rho C_v T)$.

We compute horizontally and temporally averaged temperature $\langle T \rangle_{A,t}(z)$ for 2D and 3D runs. For a 2D flow, we average T along the horizontal axis and over time during a steady state. In 3D, the corresponding averaging is performed over horizontal planes and over time. In Fig. 3(A, B), we plot $\langle T \rangle_{A,t}(z)$ for the 2D and 3D flows respectively. Interestingly, $dT(z)/dz = -g/C_p$ in the bulk, thus verifying adiabatic cooling. The reason

for this observation is as follows.

We compute the ratio of the fluid kinetic energy and internal energy, $r = K_e/I_e = (\rho u^2/2)/(\rho C_v T)$, at every grid point. For 2D simulation with $Ra = 10^9, 10^{12}, 10^{15}$, Fig. 4 illustrates the density plot of r . Figure 5 illustrates the probability distribution function of r for 2D and 3D convection. As shown in the figures, $r \rightarrow 0$, implying that the internal energy dominates the fluid kinetic energy, or $u \ll c_s$ (c_s is the sound speed). The local Mach number of the flow is predominantly very small, but it reaches a maximum value of 0.9 at some isolated locations. The time average of maximum turbulent Mach number for all Ra 's vary from 0.5 to 0.6. This feature implies that the system is near thermodynamic equilibrium in the bulk. This is the reason why compressible convection exhibits adiabaticity in the bulk even for large Ra 's [6, 12]. These results are consistent with the fact that the convective time scale, $t_{\text{conv}} = \sqrt{d/(\epsilon g)}$, is smaller than conductive time scale, $t_{\text{cond}} = d^2/\kappa$. Their ratio $t_{\text{conv}}/t_{\text{cond}} = 1/\sqrt{RaPr} \ll 1$. Note, however, that the Schwarzschild criterion does hold in the boundary layers, where the flow is dynamic.

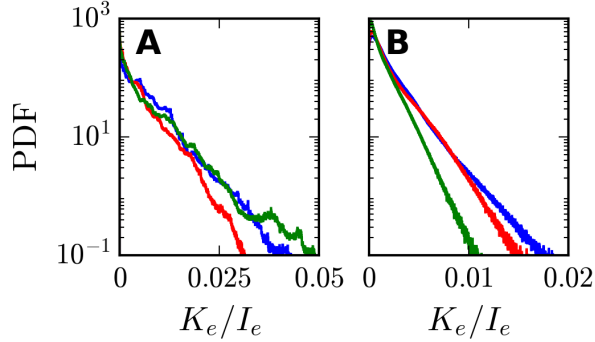


Figure 5: Normalized probability distribution function (PDF) of the ratio of the kinetic energy density, $K_e = \rho u^2/2$, and the internal energy density, $I_e = \rho C_v T$ for (A) 2D and (B) 3D convection during respective steady states. Color convention is the same as Fig. 3.

Next, we discuss the flow structures of compressible convection. Since the temperature is dominated by $T_A(z)$, we subtract it from the total temperature and plot the superadiabatic temperature $T_{\text{sa}}(\mathbf{r}) = T(\mathbf{r}) - T_A(z)$, along with the vector plots of the velocity field. These plots are illustrated in Figs. 6 and 7 for 2D and 3D flows respectively. For movies, refer to [56]. The figures and movies exhibit flow activities at the bottom and the top of the box, where the thermal plumes are generated. Note, however, that the flow velocity of the plumes is much smaller than the sound speed.

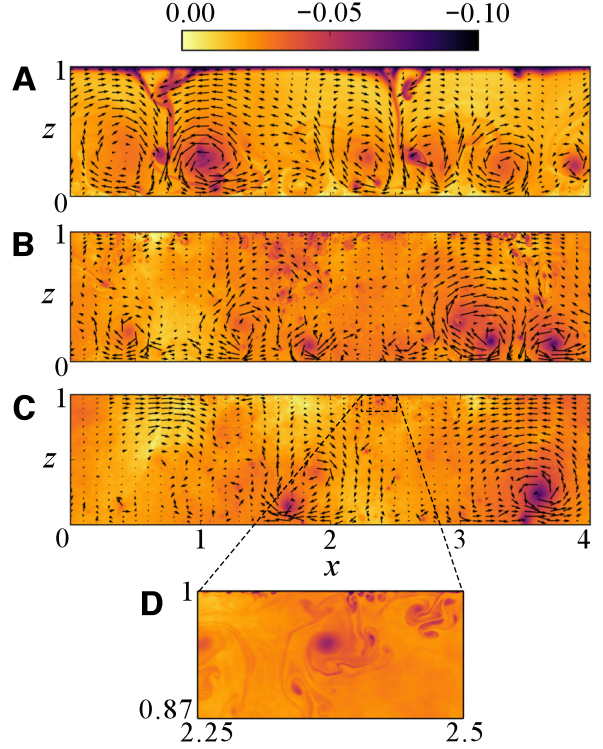
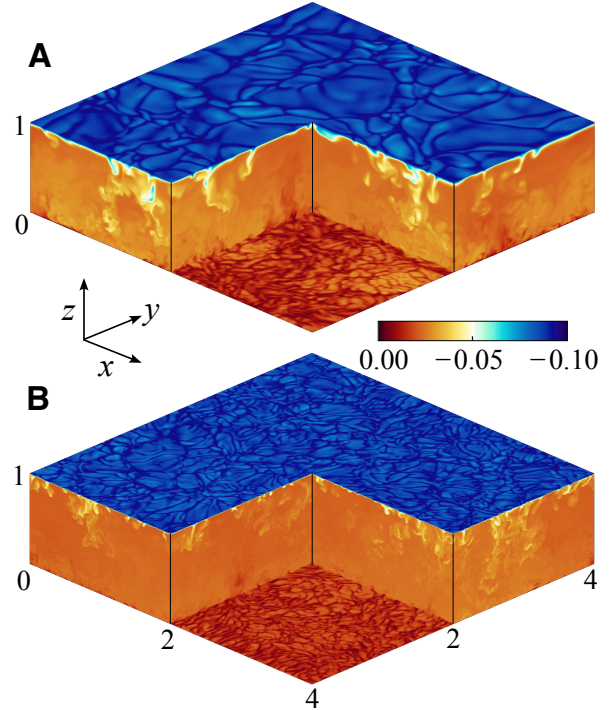


Figure 6: Plots of the velocity field \mathbf{u} and superadiabatic temperature $T_{\text{sa}}(\mathbf{r})$ for 2D convection with (A) $Ra = 10^9$, (B) $Ra = 10^{12}$, and (C) $Ra = 10^{15}$. (D) The magnified view near the top boundary for $Ra = 10^{15}$.



9 Figure 7: Plots of superadiabatic temperature $T_{\text{sa}}(\mathbf{r})$ for 3D convection at (A) $Ra = 10^9$ and (B) $Ra = 10^{11}$.

As shown in Fig. 3, the bulk temperature is nearly adiabatic, in contrast to the constant bulk temperature in RBC. Interestingly, $T_{sa} \ll T_A$ (see Figs. 6 and 7) indicating the dominance of T_A . As shown in Figs. 6 and 7), turbulent convection is more prominent near the bottom than the top, consistent with earlier findings [37, 57]. As argued by John and Schumacher [37], and Wu and Libchaber [57], the fluid is denser at the bottom than the top. Hence, using $\mu = \nu\rho = \text{const.}$, we deduce that ν and κ at the bottom are smaller than those at the top. Therefore, the bottom region has stronger turbulence with relatively thin and easily-detachable plumes than the top region [36, 57]. In the following, we discuss these boundary layer features.

5. Boundary Layers of Compressible Convection

The planar-averaged temperature $\langle T \rangle_{A,t}(z)$, exhibited in Fig. 3, shows that the temperature drops rather sharply at the top and bottom boundary layers. In Figs. 8 and 9, we plot the zoomed-view of the 2D and 3D boundary layers.

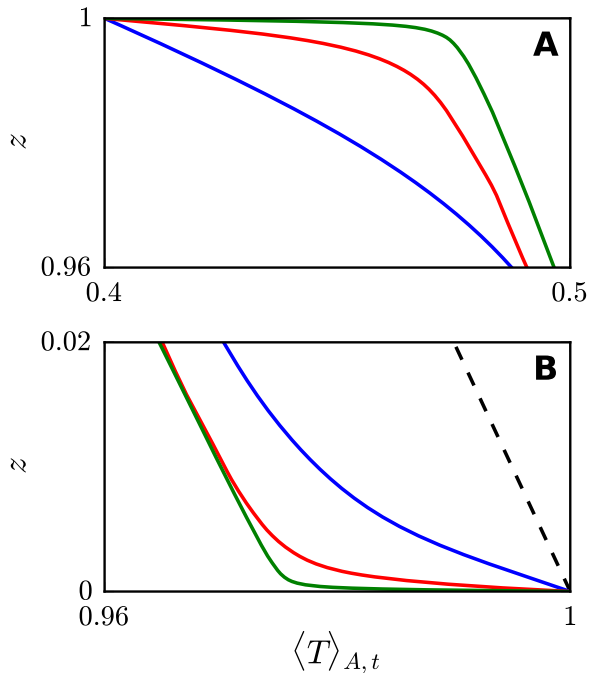


Figure 8: Boundary layers in 2D convection: The horizontally and temporally averaged $\langle T \rangle_{A,t}(z)$ in the (A) top boundary layer and (B) bottom boundary layer. Color convention is the same as Fig. 3.

Unlike RBC, in compressible convection, the top boundary layer is thicker than the bottom one. At the

bottom boundary layers of the 2D flows, the nondimensional temperature drops from 1 to 0.96 (approximately) as z increases from 0 to 0.02. However, at the top boundary layer, the temperature drops more rapidly—from 0.5 to 0.4 as z varies from 0.96 to 1. A similar temperature drop is observed in 3D flows, albeit at low Ra's. These abrupt temperature drops at the top are due to higher κ at the top than the bottom because of the density profile [37, 57]. Also note that at the top boundary layer, the rate of temperature drop increases with Ra. The above results are consistent with those of John and Schumacher [36, 37].

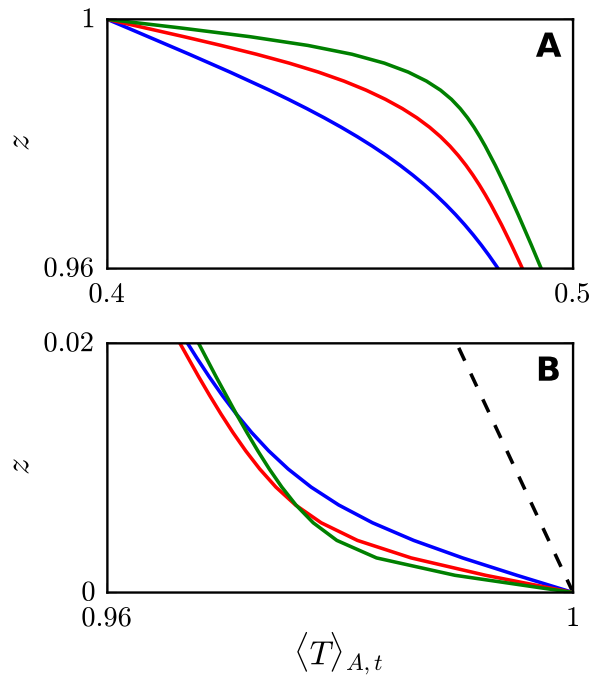


Figure 9: Boundary layers in 3D convection: $\langle T \rangle_{A,t}(z)$ in the (A) top boundary layer and (B) bottom boundary layer. Color convention is the same as Fig. 3.

We compute the thicknesses of the top and bottom boundary layers. For the same, we identify $z = \lambda_{t,b}$ where the slope of $\langle T \rangle_{A,t}$ approximates the adiabatic temperature gradient $-D$ near the top and bottom boundaries, respectively. The variation of $\lambda_{t,b}$ as a function of Ra is plotted in Fig. 10(A, B) for 2D and 3D flows. The red squares and blue circles represent the bottom and top boundary layers, respectively. It is evident that the top boundary layer is wider than the bottom boundary layer, and that the thickness of both boundary layers decrease with the increase of Ra. Interestingly, the boundary layer thickness follows a power law with Ra: $\lambda_t = (2.4 \pm 0.4)\text{Ra}^{(-0.184 \pm 0.005)}$, $\lambda_b =$

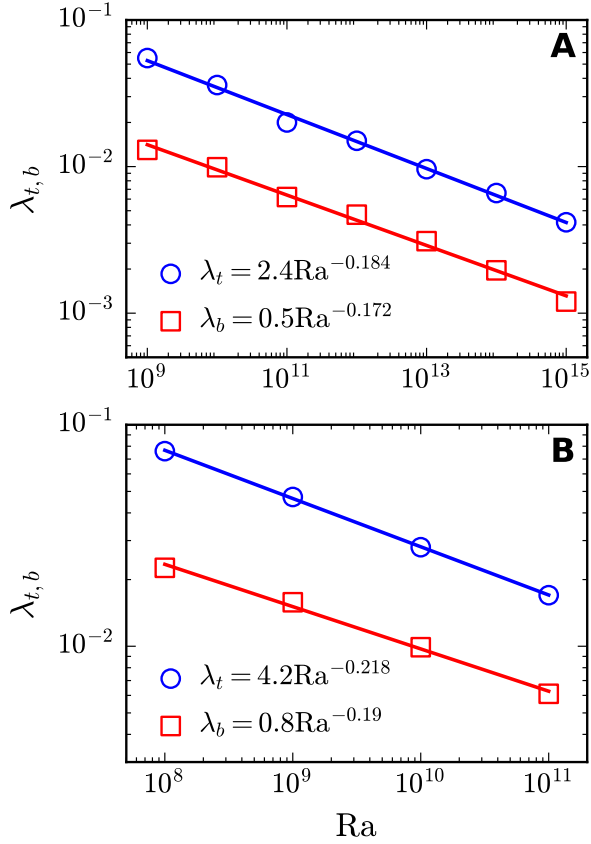


Figure 10: Plots of thermal boundary layer thicknesses $\lambda_{t,b}$ vs. Ra for (A) 2D and (B) 3D flows. The blue and red symbols depict the thicknesses of the top and bottom boundary layers for various Ra's.

$(0.5 \pm 0.1)\text{Ra}^{(-0.172 \pm 0.006)}$ for 2D, and $\lambda_t = (4.2 \pm 0.2)\text{Ra}^{(-0.218 \pm 0.003)}$, $\lambda_b = (0.8 \pm 0.2)\text{Ra}^{-0.19 \pm 0.01}$ for 3D. Note that the prefactor of λ_t is larger than that of λ_b because the top boundary layer is thicker than the bottom one. In contrast, the top and bottom boundary layers in RBC scale identically, e.g., $\lambda_t \sim \lambda_b \sim \text{Ra}^{-0.30}$ for $\text{Pr} = 1$ [58]. Thus, boundary layers of RBC and compressible convection behave very differently.

In Fig. 11 we plot the temporal and planar averaged superadiabatic temperature $T_{\text{sa}}(z) = T(z) - T_A(z)$, $\rho - \rho_A(z)$, and rms velocity $U(z)$. We observe that in the bulk, $T_{\text{sa}}(z) \approx 0$ for both 2D and 3D because the bulk temperature nearly follows adiabatic profile (see Fig. 11(A, B)). The additional temperature gradients, $dT_{\text{sa}}(z)/dz$, near the top and bottom boundary layers drive the flow. As shown in Fig. 11(A, B), $T_{\text{sa}}(z)$ nearly collapses over each other, apart from some fluctuations. As described earlier in this section, $T_{\text{sa}}(z)$ drop is greater at the top than the bottom.

Figures 11(C, D) illustrate that the density is closer

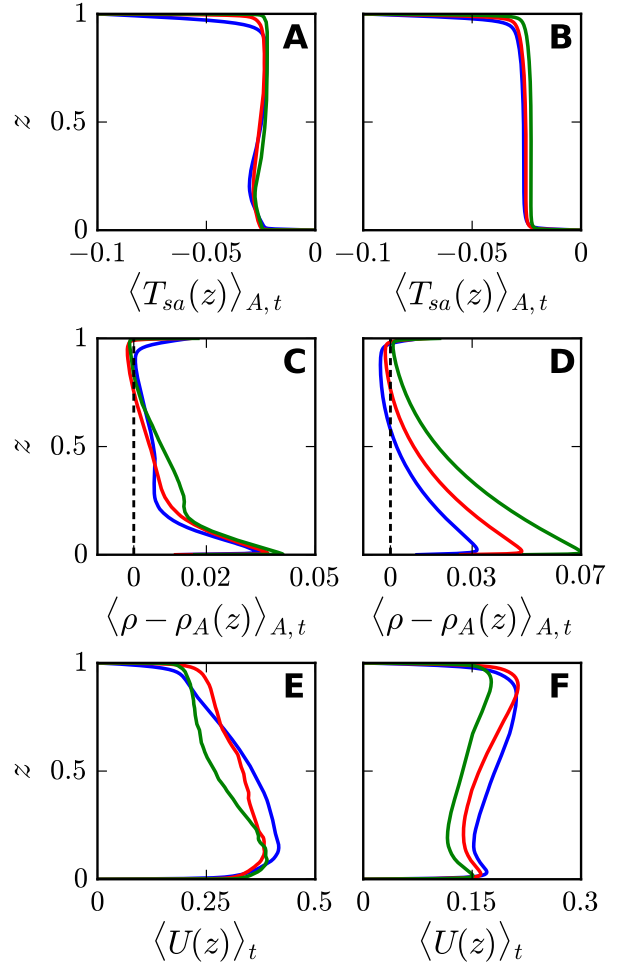


Figure 11: The planar and temporal averaged $T_{\text{sa}}(z) = T(z) - T_A(z)$ (A,B), $\rho - \rho_A(z)$ (C,D), and rms velocity $U(z)$ (E,F). The left column represents 2D flows, whereas the right column represents 3D flows. The black dashed lines in (C, D) denote adiabatic profile. Color convention is the same as Fig. 3.

to the adiabatic profile in the upper box than in the lower box. The density variations from the adiabatic profile are greater near the bottom boundary than the top one. Note that the deviation from adiabaticity for density ($\rho - \rho_A(z)$) increases with Ra, both for 2D and 3D. Figures 11(E, F) illustrate $\langle U(z) \rangle_t$ arising due to the turbulent activities. Note that $\langle U(z) \rangle_t$ decreases with increase in Ra for both 2D and 3D flows. Also, for 2D convection, $\langle U(z) \rangle_t$ at the bottom is larger than that near the top. However, it is nearly reversed in 3D. Thus, $\langle U(z) \rangle_t$ exhibits asymmetry around the mid-plane, which is unlike nearly symmetric $\langle U(z) \rangle_t$ in RBC [59].

In the next section, we will discuss Nu and Re scaling for turbulent compressible convection.

6. Nu and Re Scaling for Compressible Convection

In this section, we compute the global measures, Re and Nu, for 2D and 3D compressible convection.

6.1. Re Scaling

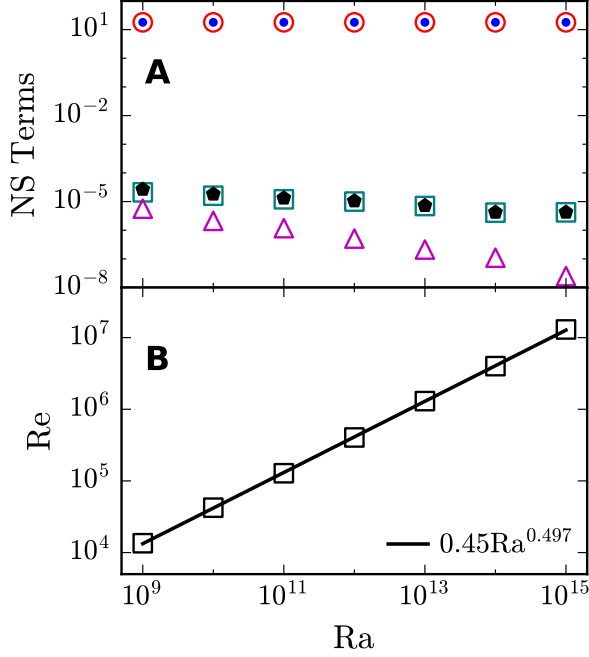


Figure 12: For 2D convection, along the z direction of the momentum equation: (A) the volume averaged $\langle F_p \rangle$ (red unfilled circles), $\langle F_b \rangle$ (blue dots), $\langle F_n \rangle$ (teal unfilled squares), $\langle F_v \rangle$ (magenta unfilled triangles), and $\langle F_b \rangle - \langle F_p \rangle$ (black pentagons); (B) the Re scaling, which is $Re \sim Ra^{0.497}$.

We analyze the relative strengths of various terms of the momentum equation along \hat{z} [Eq. (2)]. The different terms of the equation along \hat{z} are

$$\text{Nonlinear term : } F_n = \rho(\mathbf{u} \cdot \nabla)u_z, \quad (40)$$

$$\text{Pressure gradient : } F_p = -\frac{\partial p}{\partial z}, \quad (41)$$

$$\text{Buoyancy : } F_b = \rho g, \quad (42)$$

$$\text{Viscous force : } F_v = \partial_i \tau_{iz}. \quad (43)$$

We compute the volume averages of the above four terms, along with $\langle F_b \rangle - \langle F_p \rangle$. These quantities are plotted in Figs. (12A, 13A) for 2D and 3D flows respectively. The plots clearly show that

$$\langle F_p \rangle \approx \langle F_b \rangle. \quad (44)$$

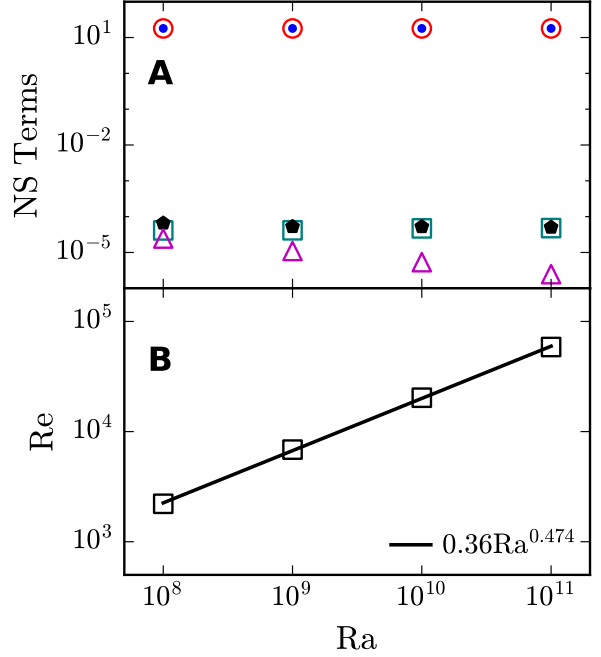


Figure 13: For 3D convection, along the z direction of the momentum equation: (A) the volume averaged $\langle F_p \rangle$ (red unfilled circles), $\langle F_b \rangle$ (blue dots), $\langle F_n \rangle$ (teal unfilled squares), $\langle F_v \rangle$ (magenta unfilled triangles), and $\langle F_b \rangle - \langle F_p \rangle$ (black pentagons); (B) the Re scaling, which is $Re \sim Ra^{0.474}$.

This balance is a key feature of *Schwarzschild criterion* [55] (see Sec. 4). Interestingly, Eq. (44) is satisfied for larger Ra's as well. This is the reason why bulk flow of compressible convection is nearly adiabatic for high Ra's as well.

It turns out that $\langle F_p \rangle$ and $\langle F_b \rangle$ do not cancel precisely, and the difference between the two terms nearly equals the nonlinear term, i.e.,

$$\langle F_n \rangle \approx \langle F_b \rangle - \langle F_p \rangle. \quad (45)$$

The viscous term, which is $\lesssim 10^{-5}$ for all Ra's, is much less than the other three terms. Using Eq. (45) we derive that

$$\frac{\tilde{\rho} \tilde{U}^2}{d} \sim \epsilon \tilde{\rho} g, \quad (46)$$

where ϵ is superadiabaticity, a small constant. Using Eq. (11) and (12), we derive that

$$Re = \frac{\tilde{U} d}{\nu} \approx \sqrt{\frac{Ra}{Pr}}. \quad (47)$$

Therefore, $Re \propto Ra^{1/2}$. We remark that the momentum equation of RBC exhibits a different balance among

various terms, with significant weight for the nonlinear term [5, 60]. Consequently, the Re scaling for the two systems are somewhat different. The relation $\text{Re} \propto \text{Ra}^{1/2}$ remains the dominant scaling for RBC as well [18], but the exponent correction may reach 0.05 for large Ra's [5, 18].

Using the 2D and 3D numerical data, we compute Re for various Ra's in the respective steady states, and list them in Table 3 (see Sec. 3.4). The listed Re's have errors ranging from 1% to 15% for the 2D flows, and from 0.5% to 2% for the 3D flows. We exhibit the Re vs. Ra plots for the 2D and 3D flows in Figs. (12B, 13B). We observe that $\text{Re} = (0.45 \pm 0.02)\text{Ra}^{(0.497 \pm 0.002)}$ for 2D, and $\text{Re} = (0.36 \pm 0.04)\text{Ra}^{(0.474 \pm 0.005)}$ for 3D. These numerical results are consistent with the prediction that $\text{Re} \propto \text{Ra}^{1/2}$.

6.2. Nu Scaling

Here, we discuss the Nu scaling. We compute the volume- and time-averaged Nu, convection-induced Nu_{conv} , and u_z -induced Nu_K using Eq. (22), as well as boundary-layer $\bar{\text{Nu}}$ using Eq. (24) for 2D and 3D runs. We employ a moving average over 10 free-fall times. The bulk Nu's, the first three quantities of the above, are listed in Table 4, whereas $\bar{\text{Nu}}$ is listed in Table 3. Note that $\bar{\text{Nu}}$, averaged over nearly 50 time units, has a maximum of 17% error for the 2D runs, but a maximum of 4% errors for the 3D runs (see Table 3 and Sec. 3.4).

Table 4: The volume- and time-averaged (over 10 free-fall times) Nu, Nu_{conv} and Nu_K of Eq. (22) for 2D and 3D runs. These quantities have significant fluctuations, especially in 2D convection. Nu_K is relatively small with large fluctuations. In the table, we do not report Nu_K for runs 2 to 5 because of large fluctuations.

Run	Ra	Nu	Nu_{conv}	Nu_K
1	10^9	21 ± 2	28 ± 2	-6 ± 2
2	10^{10}	39 ± 7	52 ± 4	-
3	10^{11}	80 ± 23	114 ± 8	-
4	10^{12}	160 ± 50	250 ± 30	-
5	10^{13}	300 ± 150	500 ± 100	-
6	10^8	13.9 ± 0.4	16.1 ± 0.5	-1.9 ± 0.7
9	10^9	27 ± 2	32 ± 2	-4 ± 1
7	10^{10}	55 ± 2	64 ± 3	-9 ± 1
8	10^{11}	110 ± 14	130 ± 15	-18 ± 2

The bulk Nu fluctuates significantly for 2D convection [61], hence we time average them over approximately 10 time units. The total Nu's have large errors, especially for large Ra's. We exclude the bulk Nu's for 2D at $\text{Ra} = 10^{14}$ and $\text{Ra} = 10^{15}$ as they exhibit more than 100% error. The errors in Nu for the 2D flows

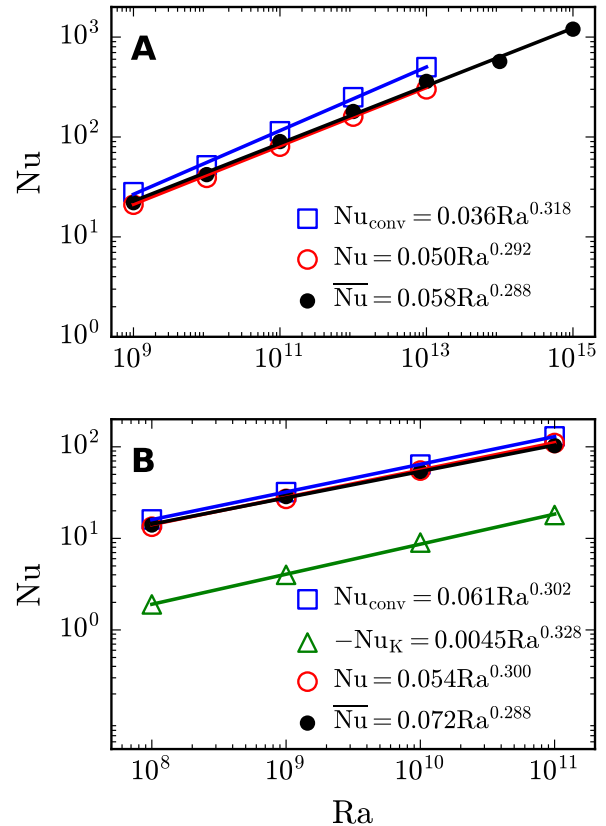


Figure 14: Nu Scaling for (A) 2D and (B) 3D convection. The figure exhibits Nu_{conv} , Nu_K , Nu, and $\bar{\text{Nu}}$ [see Eqs. (22, 24)]. Note that Nu follows near classical scaling in both 2D and 3D.

range from 10% up to 50%, but they are within 10% for the 3D flows. We observe that Nu_{conv} has similar errors as Nu, but Nu_K has relatively large errors for 2D convection. We do not list Nu_K for Runs 2 to 5 due to large errors. Fortunately, $\text{Nu}_K \ll \text{Nu}_{\text{conv}}$, hence we can ignore Nu_K safely.

In Figs. 14(A, B), we plot the averaged Nu, Nu_{conv} , and $\bar{\text{Nu}}$ for 2D and 3D flows. We also plot Nu_K for 3D flows. Interestingly, $\bar{\text{Nu}} \approx \text{Nu}$, but Nu has much larger fluctuations than $\bar{\text{Nu}}$. Also, $\text{Nu}_K \ll \text{Nu}_{\text{conv}}$ up to $\text{Ra} = 10^{13}$. Hence, in Eq. (22), the maximal contribution to Nu comes from Nu_{conv} . The fluid is denser at the bottom than near the top, which leads to $\rho u_z u^2$ being more negative than positive. Hence, $\text{Nu}_K \sim \langle \rho u_z u^2 \rangle < 0$ in compressible convection. This is unlike RBC where u_z is symmetric around the mid-plane, leading to $\langle \rho u_z u^2 \rangle = 0$ [1, 2].

Quantitatively, $\text{Nu}_{\text{conv}} = (0.036 \pm 0.007)\text{Ra}^{(0.318 \pm 0.007)}$ for 2D convection, and $(0.061 \pm 0.002)\text{Ra}^{(0.302 \pm 0.002)}$ for 3D convection. The volume-averaged Nu scales

as $(0.050 \pm 0.005)Ra^{(0.292 \pm 0.004)}$ for 2D, and $(0.054 \pm 0.003)Ra^{(0.300 \pm 0.003)}$ for 3D. We observe that \overline{Nu} follows a similar scaling as Nu . Thus, turbulent convection follows *classical scaling*, rather than *ultimate-regime scaling*.

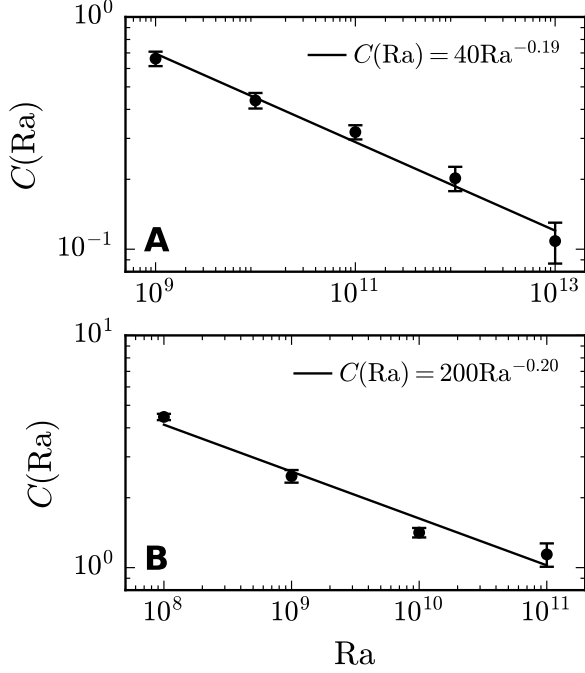


Figure 15: Plots of correlation $C(Ra)$ [Eq. (49)] for (A) 2D and (B) 3D convection. These correlations bring down the Nu scaling from $1/2$ to near 0.3 .

The above results lead to [see Eq. (22)]

$$Nu \approx Nu_{\text{conv}} \approx \langle \tilde{\rho} \tilde{u}_z \tilde{T}_{\text{sa}} \rangle \approx C(Ra) \sqrt{\langle (\tilde{\rho} \tilde{u}_z)^2 \rangle \langle \tilde{T}_{\text{sa}}^2 \rangle}, \quad (48)$$

where

$$C(Ra) = \frac{\langle \tilde{\rho} \tilde{u}_z \tilde{T}_{\text{sa}} \rangle}{\sqrt{\langle (\tilde{\rho} \tilde{u}_z)^2 \rangle \langle \tilde{T}_{\text{sa}}^2 \rangle}} \quad (49)$$

is the normalized correlation between $\tilde{\rho} \tilde{u}_z$ and \tilde{T}_{sa} . Note that $\sqrt{\langle (\tilde{\rho} \tilde{u}_z)^2 \rangle \langle \tilde{T}_{\text{sa}}^2 \rangle} \sim U \sim \sqrt{RaPr}$. The correlation $C(Ra)$ plotted in Fig. 15 reveals that $C(Ra) = (40 \pm 10)Ra^{(-0.19 \pm 0.01)}$ for 2D, and $C(Ra) = (200 \pm 100)Ra^{(-0.20 \pm 0.03)}$ for 3D. Hence, $C(Ra)$ corrects the Nu exponent from $1/2$ to near 0.3 . This feature is similar to those observed by Verma et al. [62] for RBC. However, the component Nu_K present in compressible convection, which is negative, further suppresses the Nu exponent to 0.29 in 2D and 0.3 in 3D.

Even though the dynamics of RBC and compressible convection are significantly different, the classical Re and Nu scaling are very similar. This feature is possibly due to similar $C(Ra)$ scaling in both the systems, an issue that needs a closer examination.

7. Summary

In this paper, we present simulation results of compressible convection for very high Ra 's. We simulated 2D and 3D convective flows for $Pr = 0.7$, superadiabaticity parameter $\epsilon = 0.1$, and dissipation number $D = 0.5$. We choose Ra 's in the range of 10^9 to 10^{15} in 2D, but $Ra = 10^8, 10^9, 10^{10}$ and 10^{11} in 3D. The main results reported in the paper are as follows:

1. For all our runs, the pressure gradient nearly matches with the buoyancy, thus satisfying the adiabaticity condition or Schwarzschild criterion, even for very large Ra . The density too is nearly adiabatic with the fluid density decreasing with height. We show that the adiabaticity arises because the internal energy is much stronger than the fluid kinetic energy. Hence, the flow is in quasi thermodynamic equilibrium, except near the bottom and top plates where the temperature gradients exceed g/C_p .
2. Unlike RBC, the flow and the boundary layers of compressible convection are asymmetric along the vertical. For example, the top boundary layer is thicker than the bottom boundary. With the increase in Ra , the thicknesses of both the thermal boundary layers decrease with Ra as $\sim Ra^{-0.178}$ in 2D and as $\sim Ra^{-0.2}$ in 3D.
3. For high Ra 's, the pressure gradient and buoyancy do not cancel each other exactly. The difference between the two terms nearly equals the nonlinear term. Using this feature, we derive that $Re \sim Ra^{1/2}$. Our numerical results nearly follow the above scaling.
4. We show that the Nusselt number for compressible convection exhibits near classical scaling ($Ra^{0.30}$) up to $Ra = 10^{15}$ in 2D and up to 10^{11} in 3D. Note that for RBC, several researchers [30, 27] have reported a gradual transition to the ultimate regime, which appears to be absent in compressible convection, at least up to $Ra = 10^{15}$ for 2D convection.
5. Many features of compressible convection deviate from RBC, where the temperature and the density in the bulk are nearly constant. Despite these differences, the Re and Nu scaling for compressible convection and RBC are quite similar.

Our results on compressible convection are of major importance to the atmospheres of the Earth and the Sun, both of which exhibit near adiabatic temperature profile while being turbulent. We plan to perform somewhat realistic simulations of the Earth and the Sun in near future; the latter simulation would require higher Rayleigh numbers (10^{22} to 10^{24}) and inclusion of the magnetic field. These studies would provide us valuable insights into the energetics, heat transport, and magnetic field dynamics in the Sun.

Acknowledgements

The authors thank K. R. Sreenivasan and Jörg Schumacher for useful discussions. We also thank Argonne Leadership Computing Facility (ALCF) and Oak Ridge National Laboratory (ORNL) for the computer time through the Director’s Discretionary Program. Simulations were performed on Polaris, Frontier, Param Sanganak, and our laboratory GPUs. LS acknowledges the Institute Postdoctoral Fellowship of IITK. Part of this work was supported by the Science and Engineering Research Board, India (Grant Nos. SERB/PHY/2021522 and SERB/PHY/2021473), and the J. C. Bose Fellowship (SERB /PHY/2023488).

Appendix A. Scalability of DHARA

We performed scaling analysis of DHARA (finite-difference solver) on Frontier of Oak Ridge National Laboratory (OLCF) and on Polaris of Argonne Leadership Computing Facility (ALCF). Each node of Frontier contains four AMD MI250X, each with 2 Graphics Compute Dies (GCDs), whereas each node of Polaris contains four NVIDIA A100 GPUs. On Frontier, we vary grids from 2048^3 to $16384^2 \times 2048$ and nodes from 8 to 1024. On Polaris, the corresponding grids were varied from 1024^3 to 4096^3 , and the nodes from 2 to 128.

Figure A.16(A, B) illustrate the time taken for a timestep as a function of number of nodes on Frontier and Polaris respectively. The reported time is averaged over several timesteps. We observe that the time taken $T \propto n^{-1}$, where n is the number of nodes, thus indicating strong scaling for DHARA in both systems. In addition, DHARA shows good weak scaling because the time taken remains unchanged when the grid size and number of nodes are increased proportionally.

References

[1] E. D. Siggia, “High Rayleigh number convection,” *Annu. Rev. Fluid Mech.*, vol. 26, no. 1, pp. 137–168, 1994.

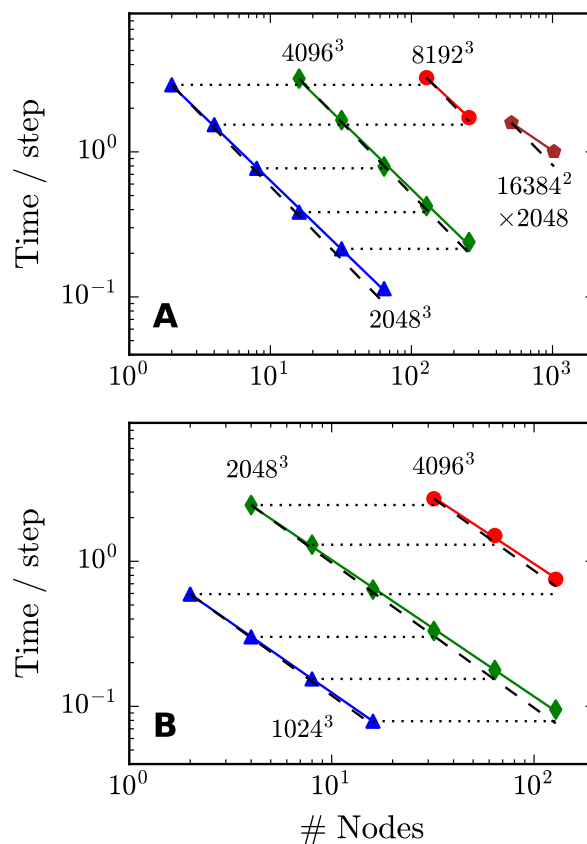


Figure A.16: Scalability of DHARA on GPUs of (A) Frontier and (B) Polaris. The figure shows the time taken per timestep vs. the number of nodes, demonstrating strong and weak scaling.

[2] G. Ahlers, S. Grossmann, and D. Lohse, “Heat transfer and large scale dynamics in turbulent Rayleigh–Bénard convection,” *Rev. Mod. Phys.*, vol. 81, pp. 503–537, Apr. 2009.

[3] D. Lohse and K.-Q. Xia, “Small-scale properties of turbulent Rayleigh–Bénard convection,” *Annu. Rev. Fluid Mech.*, vol. 42, no. 1, pp. 335–364, 2010.

[4] F. Chillà and J. Schumacher, “New perspectives in turbulent Rayleigh–Bénard convection,” *Eur. Phys. J. E*, vol. 35, no. 7, p. 58, 2012.

[5] M. K. Verma, *Physics of Buoyant Flows: From Instabilities to Turbulence*. Singapore: World Scientific, 2018.

[6] J. Schumacher and K. R. Sreenivasan, “Colloquium: Unusual dynamics of convection in the Sun,” *Rev. Mod. Phys.*, vol. 92, no. 4, p. 041001, 2020.

[7] H. C. Spruit, A. Nordlund, and A. M. Title, “Solar convection,” *Annu. Rev. Astron. Astrophys.*, vol. 28, no. 1, pp. 263–303, 1990.

[8] C. A. Jones and K. M. Kuzanyan, “Compressible convection in the deep atmospheres of giant planets,” *Icarus*, vol. 204, no. 1, pp. 227–238, 2009.

[9] E. A. Spiegel, “Convective instability in a compressible atmosphere. I,” *Astrophys. J.*, vol. 141, pp. 1068–1090, 1965.

[10] S. Chandrasekhar, *Hydrodynamic and Hydromagnetic Stability*. Clarendon: Oxford University Press, 1961.

[11] E. A. Spiegel and G. Veronis, “On the Boussinesq approximation for a compressible fluid,” *Astrophys. J.*, vol. 131, p. 442,

- 1960.
- [12] C. J. Hansen, S. D. Kawaler, and V. Trimble, *Stellar Interiors: Physical Principles, Structure, and Evolution*. New York: Springer-Verlag, 2012.
- [13] Z.-H. Wan, Q. Wang, B. Wang, S. Xia, Q. Zhou, and D.-J. Sun, "On non-Oberbeck-Boussinesq effects in Rayleigh-Bénard convection of air for large temperature differences," *J. Fluid Mech.*, vol. 889, p. A10, 2020.
- [14] A. Pandey, J. Schumacher, and K. R. Sreenivasan, "Non-Boussinesq convection at low Prandtl numbers relevant to the Sun," *Phys. Rev. Fluids*, vol. 6, no. 10, p. 100503, 2021.
- [15] A. Pandey, J. Schumacher, and K. R. Sreenivasan, "Non-Boussinesq low-Prandtl-number convection with a temperature-dependent thermal diffusivity," *Astrophys. J.*, vol. 907, no. 1, p. 56, 2021.
- [16] D. O. Gough, "The anelastic approximation for thermal convection," *J. Atmos. Sci.*, vol. 26, pp. 448–456, May 1969.
- [17] J. Verhoeven, T. Wiesehöfer, and S. Stellmach, "Anelastic versus fully compressible turbulent Rayleigh-Bénard convection," *Astrophys. J.*, vol. 805, no. 1, p. 62, 2015.
- [18] S. Grossmann and D. Lohse, "Scaling in thermal convection: a unifying theory," *J. Fluid Mech.*, vol. 407, pp. 27–56, Mar. 2000.
- [19] S. Grossmann and D. Lohse, "Thermal convection for large Prandtl numbers," *Phys. Rev. Lett.*, vol. 86, pp. 3316–3319, Apr. 2001.
- [20] B. I. Shraiman and E. D. Siggia, "Heat transport in high-Rayleigh-number convection," *Phys. Rev. A*, vol. 42, no. 6, pp. 3650–3653, 1990.
- [21] M. Lesieur, *Turbulence in Fluids*. Dordrecht: Springer-Verlag, 2008.
- [22] R. J. A. M. Stevens, E. P. van der Poel, S. Grossmann, and D. Lohse, "The unifying theory of scaling in thermal convection: the updated prefactors," *J. Fluid Mech.*, vol. 730, pp. 295–308, July 2013.
- [23] S. Bhattacharya, M. K. Verma, and A. Bhattacharya, "Predictions of Reynolds and Nusselt numbers in turbulent convection using machine-learning models," *Phys. Fluids*, vol. 34, no. 2, 2022.
- [24] M. K. Verma, A. Kumar, and A. Pandey, "Phenomenology of buoyancy-driven turbulence: recent results," *New J. Phys.*, vol. 19, p. 025012, 2017.
- [25] R. J. Samuel, M. Bode, J. D. Scheel, K. R. Sreenivasan, and J. Schumacher, "No sustained mean velocity in the boundary region of plane thermal convection," *Journal of Fluid Mechanics*, vol. 996, p. A49, 2024.
- [26] R. H. Kraichnan, "Turbulent thermal convection at arbitrary Prandtl number," *Phys. Fluids*, vol. 5, pp. 1374–1389, Nov. 1962.
- [27] D. Lohse and O. Shishkina, "Ultimate Rayleigh-Bénard turbulence," *Rev. Mod. Phys.*, vol. 96, no. 3, p. 035001, 2024.
- [28] W. V. R. Malkus, "The Heat Transport and Spectrum of Thermal Turbulence," *Proc. R. Soc. Lond. A*, vol. 225, pp. 196–212, Aug. 1954.
- [29] X. Chavanne, F. Chillà, B. Chabaud, B. Castaing, and B. Hebral, "Turbulent Rayleigh-Bénard convection in gaseous and liquid He," *Phys. Fluids*, vol. 13, pp. 1300–1320, May 2001.
- [30] X. He, D. Funfschilling, H. Nobach, E. Bodenschatz, and G. Ahlers, "Transition to the Ultimate State of Turbulent Rayleigh-Bénard Convection," *Phys. Rev. Lett.*, vol. 108, p. 024502, Jan. 2012.
- [31] X. Zhu, V. Mathai, R. J. A. M. Stevens, R. Verzicco, and D. Lohse, "Transition to the Ultimate Regime in Two-Dimensional Rayleigh-Bénard Convection," *Phys. Rev. Lett.*, vol. 120, p. 144502, Apr. 2018.
- [32] J. J. Niemela, L. Skrbek, K. R. Sreenivasan, and R. J. Donnelly, "Turbulent convection at very high Rayleigh numbers," *Nature*, vol. 404, pp. 837–840, Jan. 2000.
- [33] P. Urban, P. Hanzelka, T. Kralik, V. Musilová, A. Srnka, and L. Skrbek, "Effect of Boundary Layers Asymmetry on Heat Transfer Efficiency in Turbulent Rayleigh-Bénard Convection at Very High Rayleigh Numbers," *Phys. Rev. Lett.*, vol. 109, p. 154301, Oct. 2012.
- [34] K. P. Iyer, J. D. Scheel, J. Schumacher, and K. R. Sreenivasan, "Classical $1/3$ scaling of convection holds up to $Ra = 10^{15}$," *Proc. Natl. Acad. Sci.*, vol. 117, no. 14, pp. 7594–7598, 2020.
- [35] K. R. Sreenivasan and J. J. Niemela, "Turbulent convection at very high Rayleigh numbers and the weakly nonlinear theory," *Atmosphere*, vol. 14, no. 5, p. 826, 2023.
- [36] J. P. John and J. Schumacher, "Strongly superadiabatic and stratified limits of compressible convection," *Phys. Rev. Fluids*, vol. 8, no. 10, p. 103505, 2023.
- [37] J. P. John and J. Schumacher, "Compressible turbulent convection in highly stratified adiabatic background," *J. Fluid Mech.*, vol. 972, p. R4, 2023.
- [38] J. P. John and J. Schumacher, "Compressible turbulent convection: The role of temperature-dependent thermal conductivity and dynamic viscosity," *Phys. Fluids*, vol. 36, no. 7, 2024.
- [39] D. H. Porter and P. R. Woodward, "Three-dimensional simulations of turbulent compressible convection," *Astrophys. J. Suppl. Ser.*, vol. 127, no. 1, p. 159, 2000.
- [40] C. Ouyang, S. He, Q. Xu, Y. Luo, and W. Zhang, "A MacCormack-TVD finite difference method to simulate the mass flow in mountainous terrain with variable computational domain," *Comput. Geosci.*, vol. 52, pp. 1–10, 2013.
- [41] H. C. Yee, *Upwind and symmetric shock-capturing schemes*. National Aeronautics and Space Administration, Ames Research Center, 1987.
- [42] D. Liang, B. Lin, and R. A. Falconer, "Simulation of rapidly varying flow using an efficient TVD-MacCormack scheme," *Int. J. Numer. Methods Fluids*, vol. 53, no. 5, pp. 811–826, 2007.
- [43] J. Schmalzl, M. Breuer, and U. Hansen, "On the validity of two-dimensional numerical approaches to time-dependent thermal convection," *Europhys. Lett.*, vol. 67, pp. 390–396, Aug. 2004.
- [44] E. P. van der Poel, R. J. A. M. Stevens, and D. Lohse, "Comparison between two- and three-dimensional Rayleigh-Bénard convection," *J. Fluid Mech.*, vol. 736, pp. 177–194, Nov. 2013.
- [45] A. Pandey, M. K. Verma, A. G. Chatterjee, and B. Dutta, "Similarities between 2D and 3D convection for large Prandtl number," *Pramana-J. Phys.*, vol. 87, p. 13, June 2016.
- [46] E. Graham, "Numerical simulation of two-dimensional compressible convection," *J. Fluid Mech.*, vol. 70, no. 4, pp. 689–703, 1975.
- [47] N. E. Hurlburt, J. Toomre, and J. M. Massaguer, "Two-dimensional compressible convection extending over multiple scale heights," *Astrophys. J.*, vol. 282, pp. 557–573, 1984.
- [48] J. D. Anderson, "Governing equations of fluid dynamics," *Computational Fluid Dynamics: An Introduction*, pp. 15–51, 1992.
- [49] R. Okuta, Y. Unno, D. Nishino, S. Hido, and C. Loomis, "CuPy: A NumPy-Compatible Library for NVIDIA GPU Calculations," in *Proceedings of Workshop on Machine Learning Systems (LearningSys) in The Thirty-first Annual Conference on Neural Information Processing Systems (NIPS)*, 2017.
- [50] L. Dalcín, R. Paz, M. Storti, and J. D'Elia, "MPI for Python: Performance improvements and MPI-2 extensions," *J. Parallel Distrib. Comput.*, vol. 68, no. 5, pp. 655–662, 2008.
- [51] C. R. Harris, K. J. Millman, S. J. Van Der Walt, R. Gommers, P. Virtanen, D. Cournapeau, E. Wieser, J. Taylor, S. Berg, N. J. Smith, et al., "Array programming with NumPy," *Nature*, vol. 585, no. 7825, pp. 357–362, 2020.
- [52] R. J. A. M. Stevens, R. Verzicco, and D. Lohse, "Radial bound-

- ary layer structure and Nusselt number in Rayleigh–Bénard convection,” *J. Fluid Mech.*, vol. 643, pp. 495–507, Jan. 2010.
- [53] G. Grötzbach, “Spatial resolution requirements for direct numerical simulation of the Rayleigh–Bénard convection,” *J. Comput. Phys.*, vol. 49, no. 2, pp. 241–264, 1983.
- [54] P. K. Mishra, A. K. De, M. K. Verma, and V. Eswaran, “Dynamics of reorientations and reversals of large-scale flow in Rayleigh–Bénard convection,” *J. Fluid Mech.*, vol. 668, pp. 480–499, 2011.
- [55] L. D. Landau and E. M. Lifshitz, *Fluid Mechanics*. Course of Theoretical Physics, Oxford: Elsevier, 2nd ed., 1987.
- [56] “*The movies are available here.*” YouTube, Aug 2024.
- [57] X.-Z. Wu and A. Libchaber, “Non-boussinesq effects in free thermal convection,” *Phys. Rev. A*, vol. 43, pp. 2833–2839, Mar 1991.
- [58] S. Bhattacharya, R. Samtaney, and M. K. Verma, “Scaling and spatial intermittency of thermal dissipation in turbulent convection,” *Phys. Fluids*, vol. 31, p. 075104, July 2019.
- [59] P. K. Mishra and M. K. Verma, “Energy spectra and fluxes for Rayleigh–Bénard convection,” *Phys. Rev. E*, vol. 81, p. 056316, May 2010.
- [60] A. Pandey, A. Kumar, A. G. Chatterjee, and M. K. Verma, “Dynamics of large-scale quantities in Rayleigh–Bénard convection,” *Phys. Rev. E*, vol. 94, p. 053106, Nov. 2016.
- [61] E. P. Van Der Poel, R. Ostilla-Mónico, R. Verzicco, and D. Lohse, “Effect of velocity boundary conditions on the heat transfer and flow topology in two-dimensional Rayleigh–Bénard convection,” *Phys. Rev. E*, vol. 90, no. 1, p. 013017, 2014.
- [62] M. K. Verma, P. K. Mishra, A. Pandey, and S. Paul, “Scalings of field correlations and heat transport in turbulent convection,” *Phys. Rev. E*, vol. 85, p. 016310, Jan. 2012.